

## A new preclinical ultrasound platform for widefield 3D imaging of rodents

Tomasz J. Czernuszewicz, Virginie Papadopoulou, Juan D. Rojas, Rajalekha M. Rajamahendiran, Jonathan Perdomo, James Butler, Max Harlacher, Graeme O'Connell, Dženan Zukić, Stephen R. Aylward, Paul A. Dayton, and Ryan C. Gessner

Citation: *Review of Scientific Instruments* **89**, 075107 (2018); doi: 10.1063/1.5026430

View online: <https://doi.org/10.1063/1.5026430>

View Table of Contents: <http://aip.scitation.org/toc/rsi/89/7>

Published by the *American Institute of Physics*

---

---



## A new preclinical ultrasound platform for widefield 3D imaging of rodents

Tomasz J. Czernuszewicz,<sup>1</sup> Virginie Papadopoulou,<sup>2</sup> Juan D. Rojas,<sup>2</sup>  
Rajalekha M. Rajamahendiran,<sup>1</sup> Jonathan Perdomo,<sup>1</sup> James Butler,<sup>1</sup>  
Max Harlacher,<sup>1</sup> Graeme O'Connell,<sup>1</sup> Dženan Zukić,<sup>3</sup> Stephen R. Aylward,<sup>3</sup>  
Paul A. Dayton,<sup>2</sup> and Ryan C. Gessner<sup>1,a)</sup>

<sup>1</sup>SonoVol, Inc., Research Triangle Park, North Carolina 27709, USA

<sup>2</sup>Joint Department of Biomedical Engineering, The University of North Carolina

and North Carolina State University, Chapel Hill, North Carolina 27599, USA

<sup>3</sup>Kitware, Inc., Carrboro, North Carolina 27510, USA

(Received 19 February 2018; accepted 21 June 2018; published online 13 July 2018)

Noninvasive *in vivo* imaging technologies enable researchers and clinicians to detect the presence of disease and longitudinally study its progression. By revealing anatomical, functional, or molecular changes, imaging tools can provide a near real-time assessment of important biological events. At the preclinical research level, imaging plays an important role by allowing disease mechanisms and potential therapies to be evaluated noninvasively. Because functional and molecular changes often precede gross anatomical changes, there has been a significant amount of research exploring the ability of different imaging modalities to track these aspects of various diseases. Herein, we present a novel robotic preclinical contrast-enhanced ultrasound system and demonstrate its use in evaluating tumors in a rodent model. By leveraging recent advances in ultrasound, this system favorably compares with other modalities, as it can perform anatomical, functional, and molecular imaging and is cost-effective, portable, and high throughput, without using ionizing radiation. Furthermore, this system circumvents many of the limitations of conventional preclinical ultrasound systems, including a limited field-of-view, low throughput, and large user variability. *Published by AIP Publishing.* <https://doi.org/10.1063/1.5026430>

### INTRODUCTION

Preclinical animal models are the gold standard for basic and applied oncology research, as the complex interaction of numerous cell types during the onset and progression of tumor development is challenging to mimic using *in vitro* models.<sup>1,2</sup> Just as our ability to generate high-fidelity mouse models has progressed, so too has the need for better noninvasive imaging technologies to enable longitudinal assessment of disease presence, tissue functional status, and response to therapy within these models.<sup>3</sup> While advances in noninvasive imaging technologies have improved the quality of science done in preclinical studies and have the potential to reduce the number of animals per study, challenges remain within the preclinical imaging space regarding cost, complexity, sensitivity, and throughput, which limit the widespread use of these technologies.

There are many ways to noninvasively image an animal and evaluate the tumor presence and functional status therein. Modalities such as magnetic resonance imaging (MRI), x-ray computed tomography (CT), and ultrasound (US) are primarily anatomical in nature, enabling the visualization of gross tissue structure within the body, such as tumor size. Modalities such as bioluminescence imaging (BLI), single photon emission computed tomography (SPECT), and positron emission

tomography (PET) are primarily functional in nature, enabling the visualization of physiological events within the body, such as metabolomic processes.

In oncology, the most commonly used method of tracking tumor progression and regression is through measuring change in tumor volume, typically by utilizing conventional noninvasive imaging technologies such as MRI, CT, or US. This method has been codified via the Response Evaluation Criteria in Solid Tumors (RECIST) and is widely used in both preclinical research and the clinic.<sup>4</sup> However, various groups have demonstrated that RECIST does not always accurately reflect the effects of therapy<sup>5–9</sup> as molecular and functional changes often precede a change in gross tumor volume.

To address this need, researchers and physicians have developed numerous molecular imaging technologies, some of which are already being adopted in the clinic today. Examples of such technologies include contrast-enhanced MRI, perfusion CT, and PET, and studies have demonstrated that these methods can predict response to therapy earlier than RECIST measurements.<sup>5,10–15</sup> Contrast-enhanced ultrasound (CEUS) is another technology that has also been explored in this context and has shown success in detecting functional changes in tumors prior to volume change.<sup>16–19</sup> Using US as the underlying imaging modality to perform molecular/functional imaging confers several advantages because US is portable, does not utilize ionizing radiation, and is more cost-effective compared with the technologies mentioned above.

To perform CEUS, imaging is done in conjunction with a microbubble contrast agent (MCA) that enables quantitative

<sup>a)</sup> Author to whom correspondence should be addressed: ryan.gessner@sonovol.com. Current address: First Flight Venture Center, 2 Davis Dr., Research Triangle Park, NC 27709-3169. Telephone: 844-766-6865 x707.

measurements of blood flow, perfusion, and vascularity<sup>20–22</sup> or that can be targeted to the expression of different cell receptors.<sup>23–27</sup> CEUS has been successfully utilized to not only detect but also predict response and resistance to therapy prior to tumor volume changes in both animals and humans.<sup>28–38</sup>

While the value of preclinical US in cancer research has been repeatedly demonstrated, US (and, by extension, CEUS) is not without several limitations. First, it is known to be highly user-dependent,<sup>39</sup> a weakness likely driven by the variability surrounding the manual positioning of a 2D imaging plane within a 3D tissue volume. This necessitates highly trained sonographers with extensive knowledge of the specific equipment to obtain consistent results. Second, US is known to have a limited field-of-view (FOV). The FOV is typically confined to 2D unless the transducer is mechanically swept across the tissue, which requires external hardware. 3D acquisitions are difficult to perform for anything larger than a small sub-volume since the transducer needs to remain coupled to tissue and anatomical warping from pressure and coupling gel can cause misalignments within the 3D reconstructions. Matrix-array transducers containing multiple rows of elements are able to capture 3D scans without physically moving the transducer, but they usually have a small imaging area that is insufficient to comprehensively capture the rodent's body, are expensive, and currently lack the resolution of conventional preclinical transducers.<sup>40</sup>

Herein, we present a new instrument that attempts to address the weaknesses of both preclinical US and some of the broader challenges facing the preclinical imaging field. To mitigate the limitations of US, the system is built with a robotic gantry to control transducer positioning. This not only enables scans to extend across the animal's entire body (i.e., wide FOV) but also allows multiple mice to be scanned side-by-side in minutes, dramatically increasing the throughput of imaging studies. Finally, the system addresses the complexity of conventional US by using a simple point-and-click camera-based interface that produces consistent data even with novice operators.

As will be described in more detail in this manuscript, this new platform uses high-frequency US for anatomical imaging of tissue and acoustic angiography for both anatomical and functional CEUS imaging of vasculature. Acoustic

angiography uses the super-harmonic signal from MCAs to produce high resolution maps of vasculature with very high contrast-to-tissue ratios.<sup>41–43</sup> Acoustic angiography-derived vessel density measurements have been used in combination with destruction/reperfusion quantification to demonstrate the difference in relative blood volume between PECAM1+ tumors and PECAM1– tumors, as well as detect early response to radiation therapy.<sup>44,45</sup> To validate the system and assess imaging reproducibility, we conducted a pilot *in vivo* study evaluating tumor growth over time in a mouse xenograft model.

## METHODS

### Design of the imaging system

The imaging system was designed to allow rodents to be imaged in 3D without physical contact between the US transducer and the animal. Conventional preclinical US requires the transducer to be in contact with the tissue, which may cause the tissue to deform between frames when the transducer is swept for acquiring 3D data sets. In the proposed system, the animal is decoupled from the transducer via an acoustically transmissive membrane, while the transducer resides in a reservoir filled with a hydrocarbon fluid under the animal (Fig. 1). The reservoir allows a transducer to be manipulated beneath the animal without causing contact-induced deformations in the reconstructed 3D volume while the fluid maintains acoustic coupling. The transducer is positioned within a robotically actuated carriage driven by a custom motion stage assembly controlled through serial communication, which enables tomographic US images to be acquired over a  $5.0 \times 10.0$  cm (lateral  $\times$  elevation) FOV or greater.

While the system could be utilized with several different transducer options, the one used for these studies was a dual-element wobbler design<sup>46</sup> with the inner element centered at 24 MHz (9 mm diameter) and the outer annulus centered at 2 MHz (20 mm outer diameter and 11 mm inner diameter), both geometrically focused at 19 mm. The inner and outer transducer elements were fabricated separately out of polyvinylidene fluoride (PVDF) and lead zirconate titanate (PZT), respectively, and bonded together after a hydrophone alignment procedure. In this configuration, both high-frequency

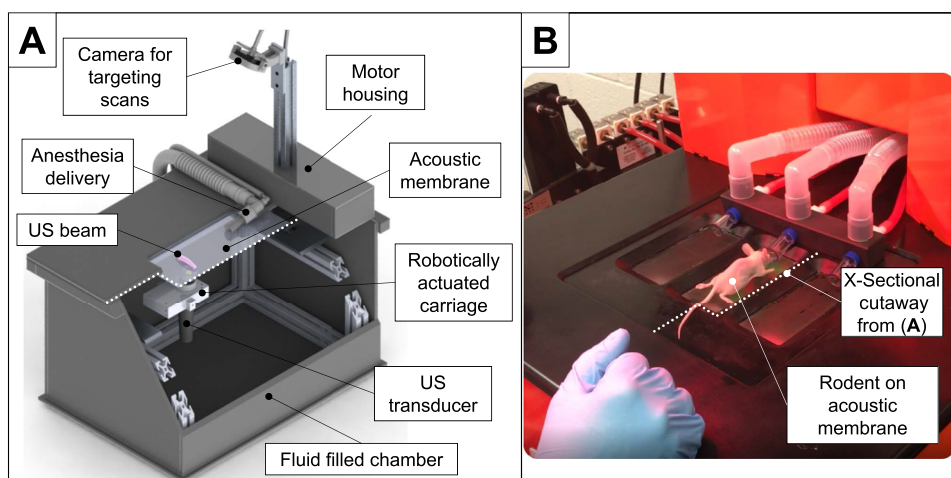


FIG. 1. Design of the imaging system. (a) Cutaway of the full system showing robotically controlled ultrasound acquisition. (b) Zoomed-in view of the top surface of the imaging system with a rodent on the imaging membrane. Cross-sectional cutaway is depicted with a dashed white line.

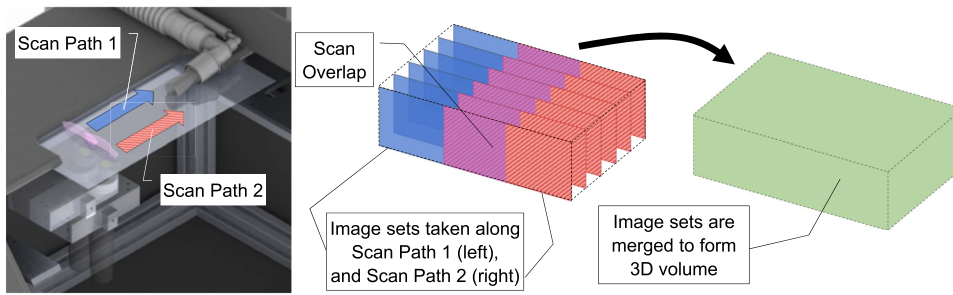


FIG. 2. Illustration of the data acquisition protocol. A transducer is mechanically translated underneath the animal in the lateral and elevational dimensions to build up a 3D volume.

B-mode and dual-frequency acoustic angiography modes can be performed for co-registered tissue and CEUS imaging, respectively. Acoustic angiography is an approach that involves transmitting a low frequency to excite a superharmonic response in MCAs which is received by the high-frequency element.<sup>41,42</sup> The transducer’s spatial location is tracked using encoders on the motors, and a camera is fixed above the animal platform to allow us scan regions of interest (ROIs) to be defined within the software. The anesthesia nose cone was positioned at the distal side of the membrane, which allowed animals to be scanned in either the prone, supine, or lateral recumbent positions depending on the anatomical features of interest [Fig. 1(b)].

**Wide-field image formation**

The lateral extent of a single US frame was 2.1 cm; so to achieve wider lateral scans than this, the transducer needed to be translated and the resulting image data stitched together (Fig. 2). To achieve a 3D reconstruction, the transducer was also translated in the elevation dimension with scan paths laterally offset by 1.4 cm, which allowed 0.7 cm of overlap (33% of frame width) between adjacent frames. A whole-abdomen FOV of a mouse could be scanned with 200 μm elevational spacing in <1 min. Images were reconstructed using a pixel-based volume reconstruction method written in C++ with linear interpolation and compounding for overlapped pixels, with reconstruction time varying depending on the number of

frames in the volume.<sup>46</sup> For the previously described two-pass scan (540 total frames), the volume reconstruction took ~20 s on a standard personal computer (PC) with Intel Core i7 3.4 GHz central processing unit (CPU).

**Camera-guided ultrasound acquisitions**

Because the US transducer is below the animal in this design, its current position relative to the anatomy of interest of a rodent on the imaging membrane is not obvious to the user. For this reason, a workflow was developed to allow users to simultaneously visualize both the position of the rodent on the membrane and the transducer’s current position. In practice, this allows a user to refer to the camera and define a region of interest (ROI) around the desired location on the mouse. In this device, only 2-axis translation was available; so scan ROI placement was limited to lateral and elevational dimensions. A typical anatomical and microvascular scan workflow is outlined in Fig. 3.

**Contrast agent formulation**

The lipid-encapsulated perfluorocarbon MCAs used in this work were manufactured in-house as previously described<sup>47</sup> and were similar to commercial lipid-shelled contrast agents (i.e., DEFINITY®). In brief, the lipids 1,2-distearoyl-sn-glycero-3-phosphocholine and 1,2-distearoyl-sn-glycero-3-phosphoethanolamine-N-methoxy (polyethylene-glycol)-2000 (DSPE-PEG2000) in a 9:1 M ratio and a total lipid

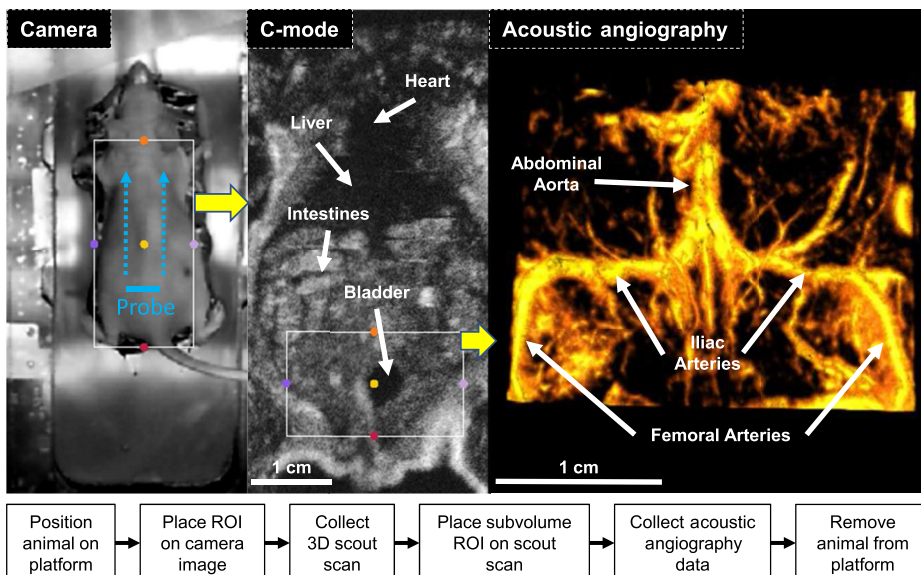


FIG. 3. Flow chart describing the image acquisition protocol. User places a region of interest (ROI) on a top-down camera image of the animal. A 3D, multi-sweep, wide-field scan is collected and visualized in the coronal plane (scanning direction shown in blue). Finally, sub-ROIs are placed to collect spatially matched, multi-modal data, including acoustic angiography.

concentration of 1.0 mg/mL were dissolved in a solution of phosphate-buffered saline, propylene glycol, and glycerol (16:3:1). Then, 1.5 mL of the solution was added to a 3-mL glass vial and the head space was gas-exchanged with Decafluorobutane gas. Microbubbles (1  $\mu\text{m}$  mean diameter and a  $1 \times 10^{10}$  #/mL concentration) were produced by using an agitation technique.

### Hydrophone measurements

Acoustic characterization of the dual-frequency transducer was carried out in a water tank at room temperature using a capsule hydrophone (HGL-0085, Onda Corp., Sunnyvale, CA) with frequency range ( $\pm 3$  dB) of 0.25–40 MHz. The hydrophone was mounted on a computer-controlled XYZ linear motion stage (Velmex Inc., Bloomfield, NY). Hydrophone signals were digitized using a 14-bit A/D card with 100 MHz sampling rate (Gage CSE8327, DynamicSignals LLC, Lockport, IL). Beam widths were estimated by fitting a circle to the  $-3$  dB contour of the lateral/elevation beamplot of each respective element.

### Animal experimental protocol

All animal procedures and protocols described in this work were approved by the University of North Carolina Institutional Animal Care and Use Committee (IACUC). Eight NOD/scid/gamma (NSG) female mice (*Mus musculus*) were injected subcutaneously in the flank with  $8 \times 10^9$  786-O human clear-cell renal cell carcinoma (ccRCC) cells. Weekly imaging commenced after tumors reached a caliper-measured size of 150 mm<sup>3</sup> and continued until tumors reached a maximum size of 1 cm<sup>3</sup> (~4-5 weeks). An additional six nude athymic female mice were injected subcutaneously in the flank with  $7 \times 10^5$  SVR angiosarcoma cells to perform an inter-operator variability study (described in more detail below).

During each imaging session, the mice were anesthetized with 1.5% isoflurane and warmed with a heat lamp to maintain body temperature. For the administration of MCAs, a 27-gauge indwelling catheter was inserted into the tail vein. MCAs were continuously infused at a rate of  $1.5 \times 10^8$  bubbles/min using a computer-controlled syringe pump, consistent with previously published infusion rates in acoustic angiography studies.<sup>42,43</sup> The relatively high infusion rate was necessary to maintain constant concentration during imaging due to the short half-life of the microbubbles (~3 min in circulation) and the pressure requirements of acoustic angiography that cause the destruction of some bubbles to achieve superharmonic response.

Imaging proceeded as outlined in the flow chart at the bottom of Fig. 3. Animals were placed in the prone position

on the acoustic membrane of the imaging system with a layer of US gel between their abdomen and the membrane. Using the scan guidance camera, a “scout scan” ROI was defined and a  $3 \times 4$  cm (lateral  $\times$  elevation) data set was captured with elevational spacing of 200  $\mu\text{m}$ . Axial height of the volumetric data set was fixed at 1.8 cm. This scan served as a reference for defining a second sub-volume ROI for the follow-up tumor microvascular scans and to provide an anatomical image for offline tumor segmentation. The sub-ROI was  $2 \times 2$  cm (lateral  $\times$  elevation). Time gain compensation (TGC) for the imaging system was set to a constant value through depth and kept the same for each animal.

After the infusion pump was activated, MCAs were given 30 s to pass down the catheter, after which acoustic angiography data were acquired. Two types of acoustic angiography data were acquired within the sub-volume: a blood vessel morphology (BVM) scan to visualize vascular remodeling occurring within and surrounding the tumor and a blood vessel density (BVD) scan to quantify the density of the tumor’s microvasculature. The BVM scan was performed with a stepped acquisition (frame spacing: 200  $\mu\text{m}$ ), with 10-frame averaging at each location. The BVD scan was performed with a continuous sweep acquisition (frame spacing: ~500  $\mu\text{m}$ ), scanning the tumor repeatedly for 16 sweeps and allowing MCAs to perfuse into the tumor for 10 s between each sweep. The 16 sweeps were then averaged to form one composite BVD image. It typically took ~10 min to complete all scans once animals were anesthetized. BVD and BVM images were rendered in 2D with a C-mode maximum intensity projection (MIP) or in 3D with scalar and gradient opacity mapping to optimize contrast at vessel interfaces.

### Segmentation and quantification

Tumor ROIs were manually defined using custom-designed 3D analysis software. Several 2D ROIs were drawn within the 3D US data, and a contour interpolation algorithm<sup>48,49</sup> was used to fill in the intermediate slices (Fig. 4). The final step was to apply a median filter (kernel size of 1 mm<sup>3</sup>) to the 3D ROI to reduce high-frequency ripples introduced by the interpolation. Segmenting a tumor typically required 2 min of the user time from start to finish. The tumor size could then be computed by counting the number of voxels contained by the ROI and multiplying by the voxel volume.

### Inter-operator and inter-reader reliability assessment

To determine the system’s ability to produce user-invariant results, both inter-operator reliability and inter-reader

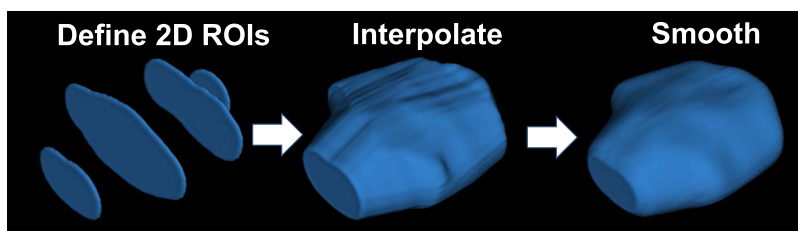


FIG. 4. Tumor segmentation workflow. The user first manually draws a number of 2D ROIs throughout the tumor volume. The intermediate slices are then interpolated and a 3D smoothing filter is applied to the resulting 3D ROI to reduce sharp transitions.

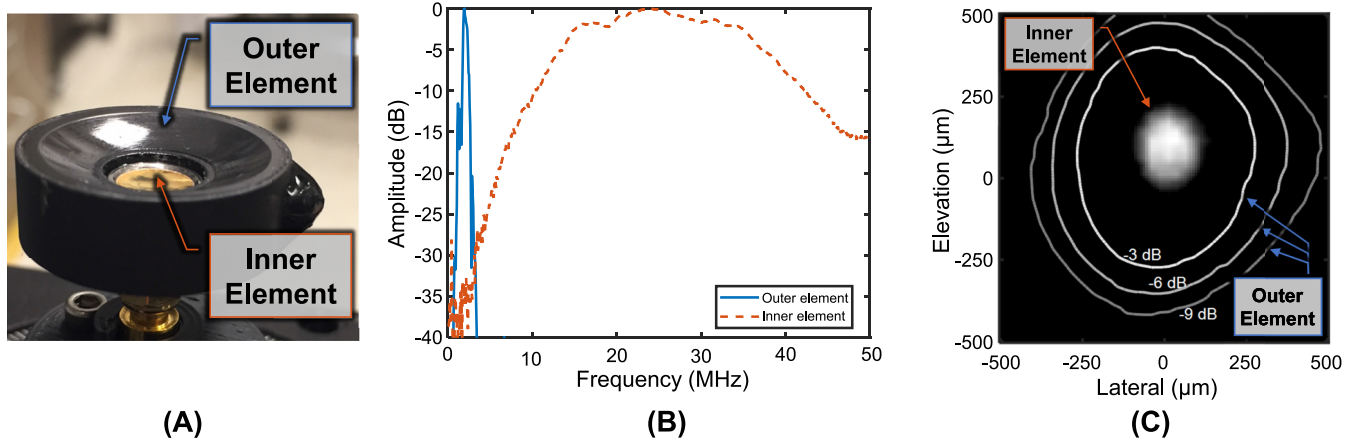


FIG. 5. Acoustic characterization of dual-frequency transducer. (a) Photograph of the transducer. (b) Normalized frequency domain plots depicting bandwidth of inner and outer elements. (c) Overlapping beam profiles the inner (gray scale image) and the outer (contour plot) elements at the focus (19 mm). Dynamic range of the inner element beamplot is 9 dB.

reliability were assessed. To determine inter-reader agreement, all tumor images from the longitudinal study captured by a single operator (V.P.) were independently segmented by 3 readers (R.C.G., J.D.R., and R.M.R.). Likewise, to determine inter-operator agreement, 3 independent operators (V.P., as well as J.K. and J.T. in the acknowledgments) acquired volumetric US images of the same mice (N = 6) on the same day sequentially. Each animal was fully repositioned by each operator and the scanning region defined by the operator. These data (N = 18 volumetric acquisitions) were segmented by the same reader (R.C.G.) to quantify variability in tumor volume resulting from different operators acquiring the data.

**Statistical analysis**

Tumor volume measurement agreement (both inter-reader and inter-operator) was quantified by calculating Krippendorff’s alpha coefficient for ratio data. The 95% confidence intervals (CI) were estimated by normal bootstrap confidence intervals<sup>50</sup> with 1000 bootstrap replicates using the “irr” and “boot” packages in Ref. 51. An alpha value of 1.0 represents perfect agreement. Additionally, Kruskal-Wallis tests were performed to determine if median tumor volumes were significantly different between the three readers at each timepoint to determine if tumor size influenced reader agreement.

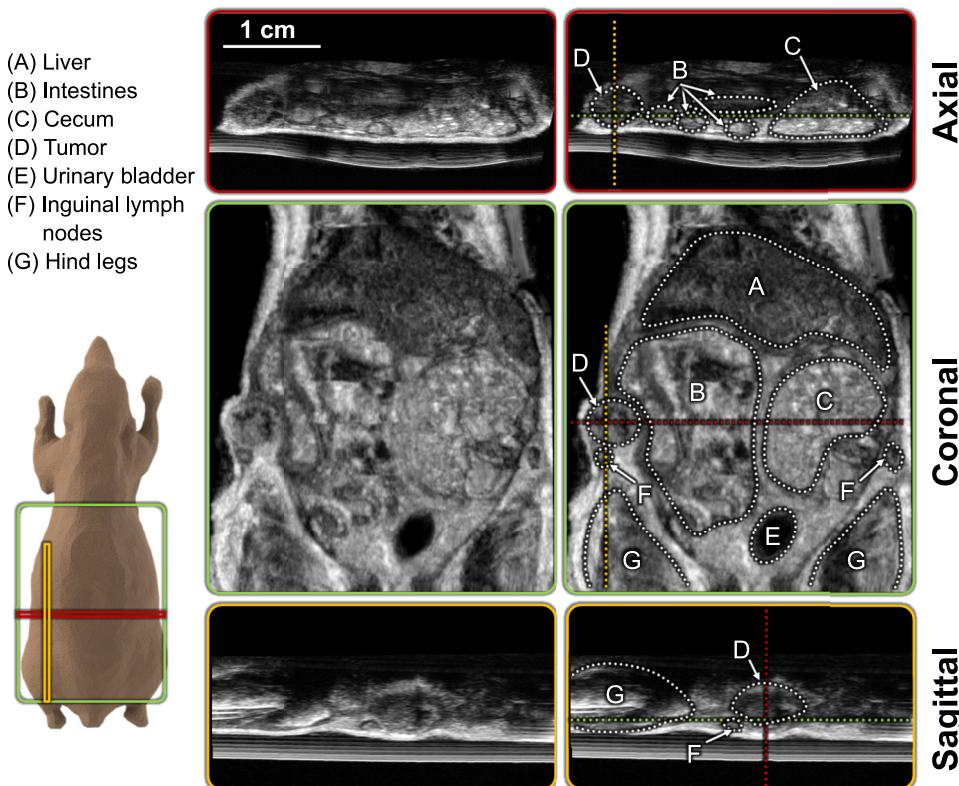


FIG. 6. Example of a wide-field abdominal scan reconstructed from 3D volumetric data. A subcutaneous tumor (65 mm<sup>3</sup>) is located in the flank of the animal (label D) located just above the inguinal lymph node. Axial, coronal, and sagittal slice locations are indicated with red, green, and yellow dotted lines. Both the original and the annotated images are provided.

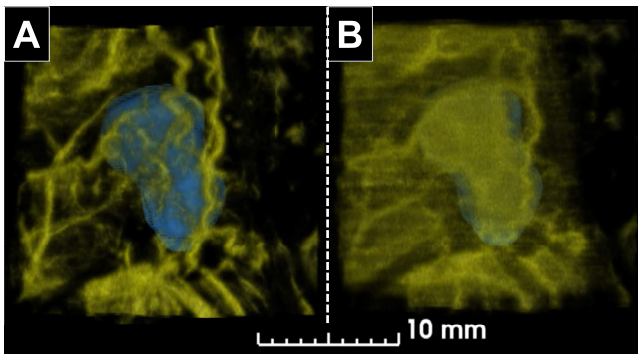


FIG. 7. Examples of the two contrast-enhanced ultrasound imaging protocols used in this study, captured on the same tumor and rendered in 3D. (a) Blood vessel morphology (BVM) scan to visualize vascular remodeling of larger vessels ( $\geq 150 \mu\text{m}$  in diameter). (b) Blood vessel density (BVD) scan showing vascularity of both large and small (i.e., sub-resolution) microvessels. Yellow indicates contrast-perfused pixels. Blue indicates manually segmented tumor boundary.

## RESULTS

Acoustic characterization of the dual-element transducer is presented in Fig. 5, which shows a photograph of the transducer [Fig. 5(a)], as well as frequency spectra [Fig. 5(b)] and lateral/elevational beam profiles at the focus [Fig. 5(c)]. The  $-3$  dB one-way bandwidths for the inner and outer elements were measured to be 86.9% (14.6–35.5 MHz) and 58% (1.54–2.69 MHz), respectively. The  $-3$  dB one-way lateral/elevational beam widths for the inner and outer elements were measured to be  $144 \mu\text{m}$  and  $601 \mu\text{m}$ , respectively.

Figure 6 shows an example of a wide-field abdominal US image reconstructed from 3D volumetric data captured with the imaging system. Many anatomical landmarks are clearly identified, including the liver, small intestines, bladder, and inguinal lymph nodes. In addition, a subcutaneous tumor in the flank of the animal is visible and readily segmented from the 3D data set. In this example, the tumor was measured to be  $65 \text{ mm}^3$ .

Figure 7 shows an example of the two CEUS imaging modes enabled by the custom dual-frequency transducer installed in the imaging system. Images were captured on the same tumor and are rendered in 3D for visualization (yellow indicates contrast-perfused regions and blue indicates tumor border, manually segmented from US volume and rendered in 3D). Figure 7(a) depicts a BVM scan to visualize the remodeling of microvessels that are at or above the imaging resolution of the system (i.e.,  $\geq 150 \mu\text{m}$  in diameter). Figure 7(b) shows a BVD scan that indicates overall perfusion and microvessel density, including sub-resolution-sized vessels. As expected, the tumor exhibits both tortuous feeder vessels and high microvessel density (as indicated by the significant enhancement on the BVD scan).

Figure 8 shows the images of the progression of a single animal's tumor over the course of 5 weeks. BVD and BVM images are rendered as 2D maximum intensity projections in the coronal plane. In the BVD images, tumor boundaries are clearly visualized as it grows in diameter from 5 mm to 10 mm. At day 31 when the tumor is  $\sim 1$  cm in diameter, an area of decreased BVD intensity appears at the center of the tumor, indicating a degradation of vascularity in that location and suggesting the development of a necrotic core. In the BVM images, multiple microvessels are observed exhibiting tortuous morphology associated with angiogenic tumors, including two vessels that are apparent across multiple time-points (arrows). Note that the number and degree of dilation of the vessels appear to increase as the tumor continues to grow over time.

Finally, Figure 9 illustrates inter-reader and inter-operator variability. For the inter-reader variability study, tumors were measured to start at a mean volume of  $\sim 200 \text{ mm}^3$ , which over the course of 5 weeks grew aggressively to reach a volume of  $\sim 1 \text{ cm}^3$ . Qualitatively, readers exhibited good agreement at each timepoint, measuring nearly the same mean tumor volume for each week and capturing the growth curve over time. This observation is reflected quantitatively in Table I, which shows alpha coefficients of 0.914 (0.824–0.948) and 0.959

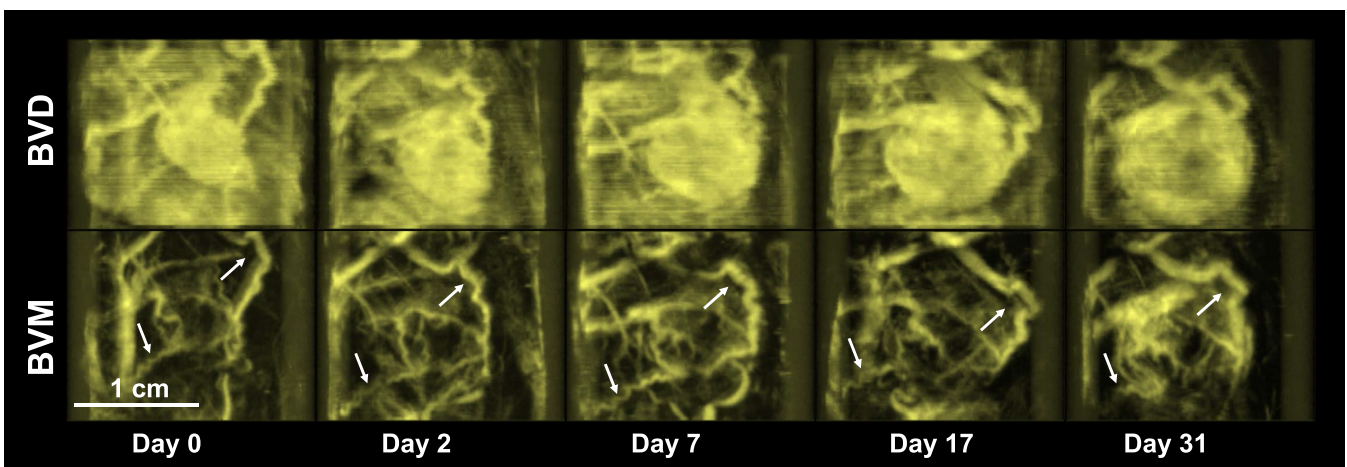


FIG. 8. Maximum intensity projections (coronal plane) of contrast-enhanced ultrasound images of a tumor growing over time. Tumor boundaries are clearly visualized in the blood vessel density (BVD) images (top row) as the highly perfused regions in the center of each frame. Blood vessel morphology (BVM) images depict tortuous vessels (arrows) that can be followed over time.

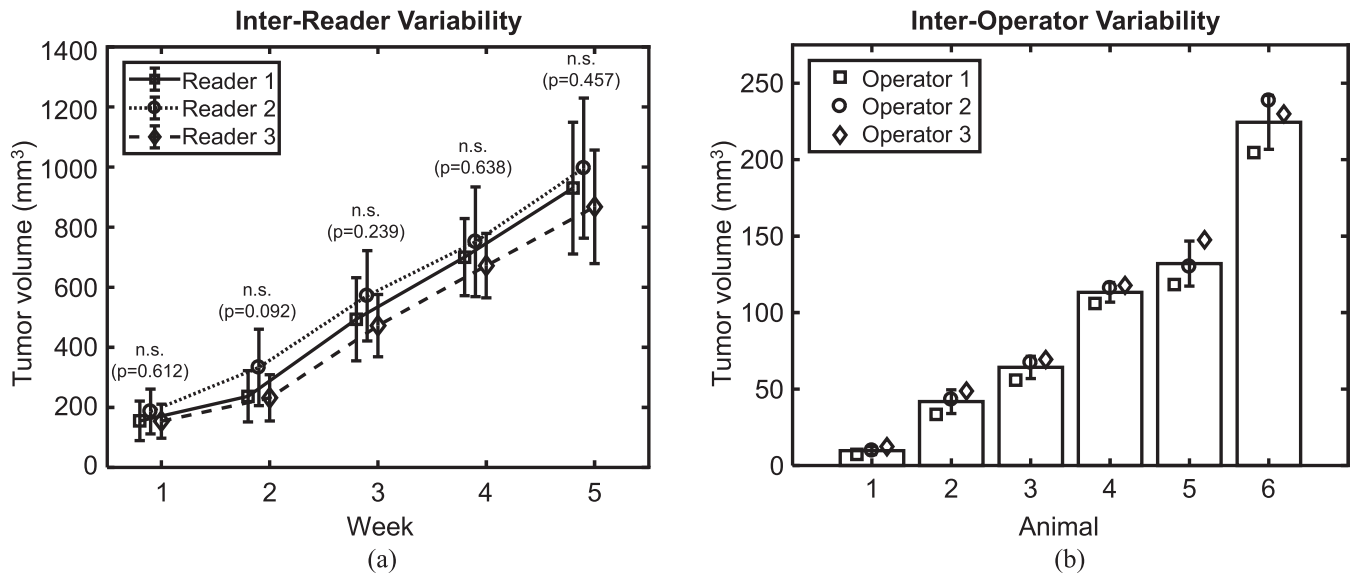


FIG. 9. Inter-reader and inter-operator variability results showing the consistency of imaging with the automated system. (a) Tumor volume versus time measured by three independent readers (data collected by one operator). (b) Tumor volume versus animal measured by one reader (data collected by three operators). P-values of the Kruskal-Wallis test for each timepoint is shown above each group when applicable. NS, not significant.

TABLE I. Inter-operator and inter-reader agreement.

	Krippendorff's alpha coefficient	95% CI
Same operator/multiple readers	0.914	(0.824–0.948)
Multiple operators/same reader	0.959	(0.911–0.981)

(0.911–0.981) for the multiple reader and multiple operator cases, respectively. Additionally, at each timepoint, no statistical difference in tumor volumes was measured across the three readers for each timepoint.

## DISCUSSION

There has been much work in recent years to develop technologies to noninvasively evaluate disease progression using preclinical imaging systems. US-based technologies specifically have the advantage of being fast and cost-effective; however, when it comes to reproducibility, FOV, throughput, and ease-of-use, the current devices have often fallen short. Here, we present a new preclinical ultrasound system that addresses these shortcomings and demonstrate a new acquisition framework that can simply and quickly capture wide-field scans of rodents, including co-registered 3D anatomical and functional images.

The advantages of this technology are two-fold: (1) by automating positioning of the transducer with robotics, the system ensures the same spatial volume is interrogated regardless of the operator and (2) by decoupling the transducer from the animal, the system can capture multiple 3D interrogations without deforming the tissue and losing co-registration of the images. This concept of multiple interrogations is similar to that of multi-parametric MRI where various pulse sequences (e.g., T1, T2, DCE) are captured one after the

other across a 3D volume and are inherently co-registered. In our device, we show the potential for measuring three parameters across a tumor using three imaging modes: tumor volume from US, tumor-vessel tortuosity from BVM, and tumor microvessel density from BVD. The captured volumes are well registered not only in the same imaging session (Fig. 7) but also across multiple timepoints spanning weeks (Fig. 8).

To quantify the degree of agreement between volume measurements, Krippendorff's alpha was calculated across two experiments, one with multiple operators and the other with multiple readers (Table I). In general, the coefficients were high, with values of 0.959 and 0.914 for multiple operators and readers, respectively, suggesting excellent agreement in both cases. As expected, the inter-operator coefficient was exceptionally high, which supports the hypothesis that robotically controlled, hands-free US acquisition can result in extremely consistent data. The inter-reader coefficient was slightly lower, suggesting that reader image-interpretation skill has a greater impact on tumor volume measurement variability than operator skill. It is expected that with additional reader training and experience, the consistency and reliability in tumor volume measurements will also increase. Nonetheless, mean tumor volumes measured for the group over time were not statistically different (Fig. 9), suggesting that tumor volume measurements from any of the three readers would lead to the same conclusions about the tumor growth rate.

The device that was demonstrated here was limited to a single fixed-focus transducer installed in a 2-axis translation carriage. The consequence of this design was that the axial depth of field and frequency range of the device were limited. While this design was sufficient to prove feasibility in subcutaneous tumors, future iterations of the device could integrate 3-axis motion and annular/linear arrays to

improve the axial depth of field. Additionally, the number of transducers in the translation carriage could be expanded to allow for seamless, ultra-wideband (15-70 MHz) preclinical imaging, without requiring a user to manually switch transducers.

Some challenges were noted during the study. As with other US-based technologies, our device required a small amount of coupling gel on the animal's torso, which was susceptible to air bubble and air-interface artifacts. Air bubbles can be mitigated by utilizing degassed gel, achieved via centrifugation, and applying a new coat of gel each time an animal is placed on the imaging pad. Air-interface artifacts arise at the skin/air juncture around the sides of the animals where there is no gel contact and can obscure the location of the skin surface. While this is not a problem for measurements of any internal organs, it can impact delineation of the boundaries of a subcutaneous tumor. In general, we found that adding a small additional amount of gel can mitigate this problem, and in the future, this artifact could be removed in software with novel clutter and reverberation rejection algorithms. Another challenge was the presence of minor discontinuities in the volumetric US image due to animal respiration or cardiac motion. The artifacts were largely not present in the tumor volumes captured in this study due to the tumors being located far from the heart and lungs in the flank and mammary pads; however, if tumors were closer to the lungs/heart, this artifact may have been more apparent and interfered with tumor segmentation. In the future, respiration and motion filtering could be used to remove these artifacts, as well as ECG gating using standard adhesive murine ECG electrodes and monitoring equipment. Additionally, in this study, we only evaluated tumor volume as a function of time. Future studies will examine microvessel density and tortuosity over time, as well as utilizing the instrument to perform response-to-therapy experiments. Finally, long-term durability studies need to be conducted to determine the lifetime of the device and maintenance requirements.

## CONCLUSION

We have demonstrated a novel preclinical ultrasound imaging system that can accurately and consistently evaluate tumors in rodent models. The system leverages cost-effective robotics technology, and the new scanning paradigm allows for easy and reproducible data acquisition to enable wide-field, 3D, multi-parametric ultrasound imaging. In future work, we will explore adding additional transducers into the system to extend its capabilities and enable advanced diagnostic modes such as ultra-wideband imaging, radiation-force elastography, targeted molecular imaging, or therapeutic modes such as high-intensity focused ultrasound (HIFU).

## ACKNOWLEDGMENTS

This work was supported in part by the National Cancer Institute (NIH/NCI Nos. R44CA165621-03 and 1F31CA196216-01) and the National Science Foundation (No. NSF-IIP-1533978). We would also like to acknowledge the University of North Carolina Animal Core for their

help during the imaging experiments, Brian Velasco for providing the lipid solution for the making of the contrast agents used in the study, as well as James Tsuruta (J.T.) and Jinwook Kim (J.K.) for participating in the operator variability study.

Several authors are either employed by or having a significant financial interest in SonoVol, Inc. (T.J.C., R.M.R., J.P., J.B., M.H., G.O., P.A.D., and R.C.G.).

- <sup>1</sup>K. Politi and W. Pao, "How genetically engineered mouse tumor models provide insights into human cancers," *J. Clin. Oncol.* **29**(16), 2273–2281 (2011).
- <sup>2</sup>M. Singh, C. L. Murriel, and L. Johnson, "Genetically engineered mouse models: Closing the gap between preclinical data and trial outcomes," *Cancer Res.* **72**(11), 2695–2700 (2012).
- <sup>3</sup>S. K. Lyons, "Imaging mouse models of cancer," *Cancer J.* **21**(3), 152–164 (2015).
- <sup>4</sup>P. Therasse, S. G. Arbuck, E. A. Eisenhauer, J. Wanders, R. S. Kaplan, L. Rubinstein *et al.*, "New guidelines to evaluate the response to treatment in solid tumors," *JNCI: J. Natl. Cancer Inst.* **92**(3), 205–216 (2000).
- <sup>5</sup>R. S. Benjamin, H. Choi, H. A. Macapinlac, M. A. Burgess, S. R. Patel, L. L. Chen *et al.*, "We should desist using RECIST, at least in GIST," *J. Clin. Oncol.* **25**(13), 1760–1764 (2007).
- <sup>6</sup>J. C. Yang, L. Haworth, R. M. Sherry, P. Hwu, D. J. Schwartzentruber, S. L. Topalian *et al.*, "A randomized trial of bevacizumab, an anti-vascular endothelial growth factor antibody, for metastatic renal cancer," *N. Engl. J. Med.* **349**(5), 427–434 (2003).
- <sup>7</sup>B. Escudier, T. Eisen, W. M. Stadler, C. Szczylik, S. Oudard, M. Siebels *et al.*, "Sorafenib in advanced clear-cell renal-cell carcinoma," *N. Engl. J. Med.* **356**(2), 125–134 (2007).
- <sup>8</sup>H. Choi, C. Charnsangavej, S. C. Faria, H. A. Macapinlac, M. A. Burgess, S. R. Patel *et al.*, "Correlation of computed tomography and positron emission tomography in patients with metastatic gastrointestinal stromal tumor treated at a single institution with imatinib Mesylate: Proposal of new computed tomography response criteria," *J. Clin. Oncol.* **25**(13), 1753–1759 (2007).
- <sup>9</sup>M. Lamuraglia, B. Escudier, L. Chami, B. Schwartz, J. Leclere, A. Roche *et al.*, "To predict progression-free survival and overall survival in metastatic renal cancer treated with sorafenib: Pilot study using dynamic contrast-enhanced Doppler ultrasound," *Eur. J. Cancer* **42**(15), 2472–2479 (2006).
- <sup>10</sup>B. Morgan, "Dynamic contrast-enhanced magnetic resonance imaging as a biomarker for the pharmacological response of PTK787/ZK 222584, an inhibitor of the vascular endothelial growth factor receptor tyrosine kinases, in patients with advanced colorectal cancer and liver metastases: Results from two Phase I studies," *J. Clin. Oncol.* **21**(21), 3955–3964 (2003).
- <sup>11</sup>H. A. Wieder, B. L. D. M. Brucher, F. Zimmermann, K. Becker, F. Lordick, A. Beer *et al.*, "Time course of tumor metabolic activity during chemoradiotherapy of esophageal squamous cell carcinoma and response of treatment," *J. Clin. Oncol.* **22**(5), 900–908 (2004).
- <sup>12</sup>P. D. Nathan, A. Vinayan, D. Stott, J. Juttla, and V. Goh, "CT response assessment combining reduction in both size and arterial phase density correlates with time to progression in metastatic renal cancer patients treated with targeted therapies," *Cancer Biol. Ther.* **9**(1), 15–19 (2010).
- <sup>13</sup>S. Stroobants, J. Goeminne, M. Seegers, S. Dimitrijevic, P. Dupont, J. Nuyts *et al.*, "18FDG-Positron emission tomography for the early prediction of response in advanced soft tissue sarcoma treated with imatinib mesylate (Glivec®)," *Eur. J. Cancer* **39**(14), 2012–2020 (2003).
- <sup>14</sup>I. Zerizer, A. Al-Nahhas, D. Towey, P. Tait, B. Ariff, H. Wasan *et al.*, "The role of early 18F-FDG PET/CT in prediction of progression-free survival after 90Y radioembolization: Comparison with RECIST and tumour density criteria," *Eur. J. Nucl. Med. Mol. Imaging* **39**(9), 1391–1399 (2012).
- <sup>15</sup>E. Frampas, N. Lassau, M. Zappa, M.-P. Vullierme, S. Koscielny, and V. Vilgrain, "Advanced hepatocellular carcinoma: Early evaluation of response to targeted therapy and prognostic value of perfusion CT and dynamic contrast enhanced-ultrasound. Preliminary results," *Eur. J. Radiol.* **82**(5), e205–e211 (2013).
- <sup>16</sup>K. Cox, J. Weeks, P. Mills, R. Chalmers, H. Devalia, D. Fish *et al.*, "Contrast-enhanced ultrasound biopsy of sentinel lymph nodes in patients with breast cancer: Implications for axillary metastases and conservation," *Ann. Surg. Oncol.* **23**(1), 58–64 (2016).
- <sup>17</sup>S. K. Kasoji, E. H. Chang, L. B. Mullin, W. K. Chong, W. K. Rathmell, and P. A. Dayton, "A Pilot Clinical Study in characterization of malignant

- renal cell carcinoma subtype with contrast-enhanced ultrasound," *Ultrason. Imaging* **39**(2), 126–136 (2016).
- <sup>18</sup>J. K. Willmann, L. Bonomo, A. Carla Testa, P. Rinaldi, G. Rindi, K. S. Valluru *et al.*, "Ultrasound molecular imaging with BR55 in patients with breast and ovarian lesions: First-in-human results," *J. Clin. Oncol.* **35**(19), 2133–2140 (2017).
- <sup>19</sup>M. Smeenge, F. Tranquart, C. K. Mannaerts, T. M. de Reijke, M. J. van de Vijver, M. P. Laguna *et al.*, "First-in-human ultrasound molecular imaging with a VEGFR2-specific ultrasound molecular contrast agent (BR55) in prostate cancer," *Invest. Radiol.* **52**(7), 419–427 (2017).
- <sup>20</sup>P. Kogan, K. A. Johnson, S. Feingold, N. Garrett, I. Guracar, W. J. Arendshorst *et al.*, "Validation of dynamic contrast-enhanced ultrasound in rodent kidneys as an absolute quantitative method for measuring blood perfusion," *Ultrasound Med. Biol.* **37**(6), 900–908 (2011).
- <sup>21</sup>V. H. J. Roberts, J. O. Lo, J. A. Salati, K. S. L. Ba, J. R. Lindner, T. K. Morgan *et al.*, "Quantitative assessment of placental perfusion by contrast-enhanced ultrasound in macaques and human subjects," *Am. J. Obstet. Gynecol.* **214**(3), 369.e1–369.e8 (2016).
- <sup>22</sup>S. Feingold, R. Gessner, I. M. Guracar, and P. A. Dayton, "Quantitative volumetric perfusion mapping of the microvasculature using contrast ultrasound," *Invest. Radiol.* **45**(10), 669–674 (2010).
- <sup>23</sup>C. Bachmann, A. L. Klibanov, T. S. Olson, J. R. Sonnenschein, J. Rivera-Nieves, F. Cominelli *et al.*, "Targeting mucosal addressin cellular adhesion molecule (MAdCAM)-1 to noninvasively image experimental Crohn's disease," *Gastroenterology* **130**(1), 8–16 (2006).
- <sup>24</sup>J. L. Tlaxca, J. J. Rychak, P. B. Ernst, P. R. Konkalmatt, T. I. Shevchenko, T. T. Pizzaro *et al.*, "Ultrasound-based molecular imaging and specific gene delivery to mesenteric vasculature by endothelial adhesion molecule targeted microbubbles in a mouse model of Crohn's disease," *J. Controlled Release* **165**(3), 216–225 (2013).
- <sup>25</sup>J. J. Rychak, J. Graba, A. M. Y. Cheung, B. S. Mystry, J. R. Lindner, R. S. Kerbel *et al.*, "Microultrasound molecular imaging of vascular endothelial growth factor receptor 2 in a mouse model of tumor angiogenesis," *Mol. Imaging* **6**(5), 289–296 (2007).
- <sup>26</sup>J. Bzyl, W. Lederle, A. Rix, C. Grouls, I. Tardy, S. Pochon *et al.*, "Molecular and functional ultrasound imaging in differently aggressive breast cancer xenografts using two novel ultrasound contrast agents (BR55 and BR38)," *Eur. Radiol.* **21**(9), 1988–1995 (2011).
- <sup>27</sup>I. Leguerney, J.-Y. Scoazec, N. Gadot, N. Robin, F. Pénault-Llorca, S. Victorin *et al.*, "Molecular ultrasound imaging using contrast agents targeting endoglin, vascular endothelial growth factor receptor 2 and integrin," *Ultrasound Med. Biol.* **41**(1), 197–207 (2015).
- <sup>28</sup>J. E. Streeter, S. G. Herrera-Loeza, N. F. Neel, J. J. Yeh, and P. A. Dayton, "A comparative evaluation of ultrasound molecular imaging, perfusion imaging, and volume measurements in evaluating response to therapy in patient-derived xenografts," *Technol. Cancer Res. Treat.* **12**(4), 311 (2013).
- <sup>29</sup>S. R. Sirsi, M. L. Flexman, F. Vlachos, J. Huang, S. L. Hernandez, H. K. Kim *et al.*, "Contrast ultrasound imaging for identification of early responder tumor models to anti-angiogenic therapy," *Ultrasound Med. Biol.* **38**(6), 1019–1029 (2012).
- <sup>30</sup>J. Zhou, H. Wang, H. Zhang, A. M. Lutz, L. Tian, D. Hristov *et al.*, "VEGFR2-targeted three-dimensional ultrasound imaging can predict responses to antiangiogenic therapy in preclinical models of colon cancer," *Cancer Res.* **76**(14), 4081–4089 (2016).
- <sup>31</sup>J. D. Rojas, F. Lin, Y.-C. Chiang, A. Chytil, D. C. Chong, V. L. Bautch *et al.*, "Ultrasound molecular imaging of VEGFR-2 in clear-cell renal cell carcinoma tracks disease response to antiangiogenic and notch-inhibition therapy," *Theranostics* **8**(1), 141–155 (2018).
- <sup>32</sup>M. Baron Toaldo, V. Salvatore, S. Marinelli, C. Palama, M. Milazzo, L. Croci *et al.*, "Use of VEGFR-2 targeted ultrasound contrast agent for the early evaluation of response to sorafenib in a mouse model of hepatocellular carcinoma," *Mol. Imaging Biol.* **17**(1), 29–37 (2015).
- <sup>33</sup>R. S. Eschbach, D.-A. Clevert, H. Hirner-Eppeneder, M. Ingrisch, M. Moser, J. Schuster *et al.*, "Contrast-enhanced ultrasound with VEGFR2-targeted microbubbles for monitoring regorafenib therapy effects in experimental colorectal adenocarcinomas in rats with DCE-MRI and immunohistochemical validation," *PLoS One* **12**(1), e0169323 (2017).
- <sup>34</sup>S. C. Baetke, A. Rix, F. Tranquart, R. Schneider, T. Lammers, F. Kiessling *et al.*, "Squamous cell carcinoma xenografts: Use of VEGFR2-targeted microbubbles for combined functional and molecular US to monitor antiangiogenic therapy effects," *Radiology* **278**(2), 430–440 (2016).
- <sup>35</sup>H. Wang, O. F. Kaneko, L. Tian, D. Hristov, and J. K. Willmann, "Three-dimensional ultrasound molecular imaging of angiogenesis in colon cancer using a clinical matrix array ultrasound transducer," *Invest. Radiol.* **50**(5), 322–329 (2015).
- <sup>36</sup>M. A. Pysz, S. B. Machtaler, E. S. Seeley, J. J. Lee, T. A. Brentnall, J. Rosenberg *et al.*, "Vascular endothelial growth factor receptor type 2-targeted contrast-enhanced US of pancreatic cancer neovasculature in a genetically engineered mouse model: Potential for earlier detection," *Radiology* **274**(3), 790–799 (2015).
- <sup>37</sup>H. Wang, A. M. Lutz, D. Hristov, L. Tian, and J. K. Willmann, "Intra-animal comparison between three-dimensional molecularly targeted US and three-dimensional dynamic contrast-enhanced US for early antiangiogenic treatment assessment in colon cancer," *Radiology* **282**(2), 443–452 (2017).
- <sup>38</sup>J. Zhou, H. Zhang, H. Wang, A. M. Lutz, A. El Kaffas, L. Tian *et al.*, "Early prediction of tumor response to bevacizumab treatment in murine colon cancer models using three-dimensional dynamic contrast-enhanced ultrasound imaging," *Angiogenesis* **20**, 547–555 (2017).
- <sup>39</sup>M. X. Tang, H. Mulvana, T. Gauthier, A. K. P. Lim, D. O. Cosgrove, R. J. Eckersley *et al.*, "Quantitative contrast-enhanced ultrasound imaging: A review of sources of variability," *Interface Focus* **1**(4), 520–539 (2011).
- <sup>40</sup>L. F. Gonçalves, J. Espinoza, J. P. Kusanovic, W. Lee, J. K. Nien, J. Santolaya-Forgas *et al.*, "Applications of 2-dimensional matrix array for 3- and 4-dimensional examination of the fetus: A pictorial essay," *J. Ultrasound Med.* **25**(6), 745–755 (2006).
- <sup>41</sup>R. C. Gessner, C. B. Frederick, F. S. Foster, and P. A. Dayton, "Acoustic angiography: A new imaging modality for assessing microvasculature architecture," *Int. J. Biomed. Imaging* **2013**, 936593.
- <sup>42</sup>R. C. Gessner, S. R. Aylward, and P. A. Dayton, "Mapping microvasculature with acoustic angiography yields quantifiable differences between healthy and tumor-bearing tissue volumes in a rodent model," *Radiology* **264**(3), 733–740 (2012).
- <sup>43</sup>S. E. Shelton, Y. Z. Lee, M. Lee, E. Cherin, F. S. Foster, S. R. Aylward *et al.*, "Quantification of microvascular tortuosity during tumor evolution using acoustic angiography," *Ultrasound Med. Biol.* **41**(7), 1896–1904 (2015).
- <sup>44</sup>J. M. Dunleavy, L. Xiao, J. Thompson, M. M. Kim, J. M. Shields, S. E. Shelton *et al.*, "Vascular channels formed by subpopulations of PECAM1(+) melanoma cells," *Nat. Commun.* **5**, 5200 (2014).
- <sup>45</sup>S. K. Kasoji, J. N. Rivera, R. C. Gessner, S. X. Chang, and P. A. Dayton, "Early assessment of tumor response to radiation therapy using high-resolution quantitative microvascular ultrasound imaging," *Theranostics* **8**(1), 156–168 (2018).
- <sup>46</sup>A. Lasso, T. Heffter, A. Rankin, C. Pinter, T. Ungi, and G. Fichtinger, "PLUS: Open-source toolkit for ultrasound-guided intervention systems," *IEEE Trans. Biomed. Eng.* **61**(10), 2527–2537 (2014).
- <sup>47</sup>J. E. Streeter, R. Gessner, I. Miles, and P. A. Dayton, "Improving sensitivity in ultrasound molecular imaging by tailoring contrast agent size distribution: *In vivo* studies," *Mol. Imaging* **9**(2), 87–95 (2010).
- <sup>48</sup>A. B. Albu, T. Beugeling, and D. Laurendeau, "A morphology-based approach for interslice interpolation of anatomical slices from volumetric images," *IEEE Trans. Biomed. Eng.* **55**(8), 2022–2038 (2008).
- <sup>49</sup>D. Zukić, J. Vicory, M. McCormick, L. Wisse, G. Gerig, P. Yushkevich *et al.*, "ND morphological contour interpolation," *Insight J.* 1–8 (2016), see <http://hdl.handle.net/10380/3563>.
- <sup>50</sup>K. Krippendorff, *Content Analysis: An Introduction to its Methodology*, 3rd ed. (SAGE Publications Inc., Thousand Oaks, 2012).
- <sup>51</sup>The R project for statistical computing, R foundation for statistical computing.